Multi-Transition Study of M51's Molecular Gas Spiral Arms

E. Schinnerer

MPI for Astronomy, Königstuhl 17, 69117 Heidelberg, Germany

A. Weiß

MPI for Radioastronomy, Auf dem Hügel 69, 53121 Bonn, Germany

S. Aalto

Chalmers University of Technology, Department of Radio and Space Science, SE-412 96 Göteborg, Sweden

and

N.Z. Scoville

California Institute of Technology, MC 249-17, Pasadena, CA 91125, U.S.A.

ABSTRACT

Two selected regions in the molecular gas spiral arms in M 51 were mapped with the Owens Valley Radio Observatory (OVRO) mm-interferometer in the ^{12}CO(2 − 1), ^{13}CO(1 − 0), C^{18}O(1 − 0), HCN(1-0) and HCO+(1-0) emission lines. The CO data have been combined with the ^{12}CO(1 − 0) data from Aalto et al. (1999) covering the central 3.5 kpc to study the physical properties of the molecular gas. All CO data cubes were short spacing corrected using IRAM 30m (^{12}CO(1 − 0): NRO 45m) single dish data. A large velocity gradient (LVG) analysis finds that the giant molecular clouds (GMCs) are similar to Galactic GMCs when studied at 180 pc (120 pc) resolution with an average kinetic temperature of T_{kin} = 20(16) K and H_2 density of n(H_2) = 120(240) cm^{-3} when assuming virialized clouds (a constant velocity gradient $\frac{dv}{dr}$). The associated conversion factor between H_2 mass and CO luminosity is close to the Galactic value for most regions analyzed. Our findings suggest that the GMC population in the spiral arms of M 51 is similar to those of the Milky Way and therefore the strong star formation occurring in the spiral arms has no strong impact on the molecular gas in the spiral arms. Extinction inferred from the derived H_2 column density is very high (A_V about 15 - 30 mag), about a factor of 5-10 higher than the average value derived toward HII regions. Thus a significant fraction of the ongoing star

formation could be hidden inside the dust lanes of the spiral arms. A comparison of MIPS 24μm and Hα data, however, suggests that this is not the case and most of the GMCs studied here are not (yet) forming stars. We also present low (4.5") resolution OVRO maps of the HCN(1-0) and HCO+(1-0) emission at the location of the brightest ^{12}CO$(1-0)$ peak.

Subject headings: galaxies: ISM — ISM: molecules — radio lines: ISM — galaxies: individual(NGC 5194)

1. Introduction

Since the first discovery of giant molecular clouds (GMCs) in our Galaxy, a major aim has been to understand their range of physical properties and their dependence on environment. Recently, Bolatto et al. (2008) showed that the GMC properties are remarkably similar over a large range of environments using a large set of interferometric observations of local dwarf galaxies as well as M31 and M33. Most studies of spiral galaxies outside the Local Group were undertaken using single dish observations where the GMCs are no longer resolved. Thus it is not obvious if the results of these studies can be directly applied to the GMC population present in these galaxies. Detailed analysis of the molecular gas at roughly GMC-scale resolution were only obtained for the centers of a few nearby galaxies such as IC 342, Maffei 2 and M 82 (Meier & Turner 2001; Meier et al. 2008; Weiß et al. 2001) all suggesting that the properties of these GMCs differ from those found in galaxy disks by exhibiting higher kinetic temperatures and lower conversion factors likely due to the effect of the more vigorous star formation present in the centers of these galaxies. Thus it would be interesting to know whether GMCs residing in galactic disks with enhanced star formation are similar to local GMCs or closer to those found in the central regions of external galaxies.

The Whirlpool galaxy M 51 is an ideal target being one of the closest (D=8.4 Mpc with 1" $\sim$ 40.7 pc; Feldmeier et al. 1997) almost face-on grand-design spiral galaxies. A significant fraction of its molecular gas is found in the spectacular spiral arms (e.g. Scoville & Young 1983; Aalto et al. 1999; Shetty et al. 2007; Koda et al. 2009). Therefore it offers an unique opportunity to study the physical properties of the molecular gas within the spiral arms. For example, Kramer et al. (2005) combined single dish data with observations from ISO to investigate the state of the interstellar medium (ISM) in the center and selected arm regions finding indications that the ISM in M 51 might differ from that of the Galaxy as most of the [CII] line emission in M 51 can be explained by arising from a photon-dominated region (PDR) unlike the 50% assumed for the Galaxy. Due to M51's low inclination ($i \sim 20^o$) non-circular motions can be more easily separated from the galactic rotation. The unusually

large streaming motions (60 - 150 km s^{-1}) found in M 51 imply a very strong density wave whose general features are velocity discontinuities and streaming across the spiral arms (e.g. Roberts & Stewart 1987).

Besides the large number of Giant Molecular Cloud Associations (GMAs) (up to 16 within one spiral arm, Aalto et al. 1999), numerous star clusters and HII regions reside in the spiral arms as is obvious in high resolution HST imaging (e.g. Scoville et al. 2001). These populations have been extensively studied using HST data (e.g. Bastian et al. 2005; Lee et al. 2005; Scheepmaker et al. 2009, and references therein). Two interesting results in the context of this paper are that younger clusters show higher extinction and are located closer to spiral arms.

The paper is organized as follows, the observations are presented in §2 while the data are described in §3. A non-LTE analysis of the spectral lines is given in §4. The relation between the GMC properties and star formation is investigated in §5. A general discussion (§6) and a summary of the findings (§7) are provided at the end.

2. Observations

2.1. Millimeter Interferometric Observations

For this multi-transition study of the molecular gas spiral arms in M 51a, two prominent regions (Fig. 1) were selected based on the interferometric map of the ^{12}CO(1 − 0) line emission obtained earlier with the Owens Valley Radio Observatory (OVRO) mm-interferometer (Aalto et al. 1999): (a) the region containing the brightest ^{12}CO(1 − 0) peak (hereafter: west), and (b) the region showing evidence for shear across a spiral arm south of the nucleus (hereafter: south) comprised of the GMAs A8, A9, and A10 (nomenclature following Rand & Kulkarni 1990). Each region was covered by a single pointing with the OVRO interferometer, and both regions are in the M1 spiral arm. The coordinates of the pointing centers are given in Tab. 1. We observed the following key tracers for molecular gas: ^{12}CO(2 − 1), ^{13}CO(1−0), C^{18}O(1−0), HCN(1-0) and HCO+(1-0). In order to accommodate simultaneous observations of the lines of ^{13}CO(1−0) and C^{18}O(1−0) as well as HCN(1-0) and HCO+(1-0), the spectral set-up for the southern and western pointing was centered at slightly different velocities. Tab. 2 lists the velocity of the central channel as well as the resolution adopted for the data analysis. The data were obtained between January 2001 and March 2002 in the C, L, E, and H configuration (for details see Tab. 3). J1159+292 and/or J1310+323 served as phase calibrators and were observed every 20min between source observations. For passband calibration 3C273, 3C84, and/or 3C345 were used. Observations of Neptune or

Uranus were observed in several tracks throughout the observing period and allowed the flux calibration of the phase calibrator which was when interpolated for the M51 observations. The uncertainty of the absolute flux calibration is about 10% (15%) at 3mm (1mm). The calibration of the *uv* data was done using the OVRO software MMA (Scoville et al. 1994). For mapping and CLEANing we used the software package MIRIAD (Sault et al. 1995). The FWHM of the primary beam of the OVRO interferometer is about 60″ (38″) at 3mm (1mm).

In addition to the new observations, we use the ^{12}CO$(1-0)$ mosaic obtained by Aalto et al. (1999). The mosaicked map consists of 19 pointings observed in the C, L and H configuration with OVRO. The final spectral resolution is 7.8 km s^{-1} with 33 channels centered at a velocity of v_{LSR} = 472 km s^{-1}. The sensitivity of the naturally (uniform) weighted data is 19 mJy beam^{-1} (25 mJy beam^{-1}) with a beam of $3.9'' \times 3.3''$ ($2.9'' \times 2.1''$). A complete description of the dataset is given by Aalto et al. (1999).

2.2. Millimeter Single Dish Observations

For a meaningful comparison of the different tracers of the molecular gas, the interferometric data need to be corrected for missing short spacings (SSC - short spacing correction). Therefore, we observed the regions of the western and southern OVRO pointings with the IRAM 30m to obtain total power data. Around each pointing center a region of $80'' \times 80''$ was mapped in the On-The-Fly (OTF) mode in July 2001. The observations were carried out using the AB receiver combination in two frequency setups covering simultaneously the ^{13}CO$(1-0)$ and ^{13}CO$(2-1)$ or the C^{18}O$(1-0)$ and ^{13}CO$(2-1)$ lines in dual-polarization mode at 3 and 1mm. Since we did not observe the ^{13}CO$(2-1)$ line at OVRO, the 1 mm data will not be described in the following.

The telescope beam size at the 3mm observing frequencies is 22″. We used four of the 1 MHz filter-banks as spectral back-ends. Each unit has 256 channels resulting in a velocity resolution of 2.6 km s^{-1} and a total velocity coverage of 670 km s^{-1} at 3mm, respectively. System temperatures were typically $\approx$170 K (T_A^*) for both frequency setups. Pointing was checked frequently and was found to be stable to within 3″. Calibration was done every 15 min using the hot/cold–load absorber measurements. The OTF observations were done in equatorial coordinates, alternating the two orthogonal scanning directions. The scan speed was $2''/s$ with a dump time of 2 s and steps orthogonal to the scanning direction of 4″ yielding spectra spaced by 4″ on sky. Data were reduced using the CLASS software. Linear baselines were subtracted from each spectrum and intensities were converted to main beam brightness temperatures ($T_{\rm mb}$). The calibrated, baseline-subtracted spectra were used to produce a 3-D data cube. During the gridding we reduced the velocity resolution to 5 km s^{-1}

for both lines. The resulting rms noise level for ^{13}CO$(1-0)$ is 9 mK in both regions. For the C^{18}O$(1-0)$ line we achieved an rms noise of 6 mK in the west and 12 mK in the south. We estimate fluxes are accurate to $\pm 10\%$.

For the SSC of the OVRO mosaic of the ^{12}CO$(1-0)$ data from Aalto et al. (1999) and our OVRO ^{12}CO$(2-1)$ observations, we used the ^{12}CO$(1-0)$ and ^{12}CO$(2-1)$ single dish maps obtained with the NRO 45m telescope (Nakai et al. 1994)[1] and the HERA receiver array at the IRAM 30m telescope (Schuster et al. 2007), respectively. The ^{12}CO$(1-0)$ data cube has spatial resolutions of $16''$ and a spatial gridding of $7.5''$ on sky for the region of interest here. The ^{12}CO$(2-1)$ data cube was observed in OTF (On-The-Fly) mode and has a spatial resolution of $11''$ and a spatial gridding of 7". The rms noise levels at the resampled spectral resolution of 5.3 km s^{-1} and 4.5 km s^{-1} is 60 mK and 30 mK ($T_{\rm mb}$) for the ^{12}CO$(1-0)$ and ^{12}CO$(2-1)$ line, respectively. We have checked and corrected the astrometry of the single-dish maps relative to the OVRO maps by comparing the peaks in the integrated intensity maps before the short spacing correction. For all maps the astrometry turned out to be consistent within the pointing errors of the single-dish observations with applied shifts of $(\delta{\rm RA} = 4.5'', \delta{\rm DEC} = -1.5'')$ and $(\delta{\rm RA} = 3.2'', \delta{\rm DEC} = 0.0'')$ for the ^{12}CO$(1-0)$ and ^{12}CO$(2-1)$ line, respectively.

2.3. Short Spacing Correction

In order to recover the flux resolved out by the interferometer (missing flux), we combined the OVRO interferometric and single dish data following the short spacing correction (SSC) method outlined by Weiß et al. (2001). In brief, this method uses the cleaned interferometer map as a starting point and replaces the central part of the *uv*-plane with visibilities calculated from the single dish map using the same spatial and velocity grid and flux units as the interferometer map. The method requires knowledge of the interferometer clean beam and the single dish beam (which has been approximated by a Gaussian). The method has no free parameters except the choice which part of the *uv*-plane is replaced by the single dish data. All visibilities shorter than the smallest projected baseline of the interferometer data were taken from Fourier transforms of the single dish data cubes. For the analysis, we produced short spacing corrected data cubes at $4.5''$ ($2.9''$) for both (west only) regions. We find that the missing flux in the OVRO pointings is ~ 50, 40 and 20% for the ^{12}CO$(1-0)$, ^{13}CO$(1-0)$ and C^{18}O$(1-0)$ lines, respectively, and $\sim 70\%$ for the ^{12}CO$(2-1)$ line. The missing flux percentage is lower towards the strong emission peaks in the interferometer

[1] http://www.nro.nao.ac.jp/∼nro45mrt/COatlas/

maps. All maps presented in the following are the short spacing corrected versions.

2.4. HST Archival Data

For comparison to sites of recent star formation we use archival HST data from the WFPC2 camera in the V band and Hα line as well as the NICMOS Paα line as presented by Scoville et al. (2001).

3. The molecular ISM

In order to study the molecular gas emission, we created moment maps from the short spacing corrected data cubes using the GIPSY (Groningen Image Processing System) task 'moment'. We used a 3σ (5σ) or 5σ (7σ) limit and required that emission above this threshold is present in at least two adjacent channels to minimize the noise for the intensity maps (velocity fields). Note that this is a very strict cut and low level emission will be missed by the moment maps presented here.

3.1. CO Morphology

Strong line emission has been detected from the ^{12}CO(1−0), ^{12}CO(2−1), and ^{13}CO(1−0) transition while C^{18}O$(1-0)$ is only detected at a low level in some smaller peaks (see Fig. 2, 3 and 4). However, the relative brightness of peaks within the arms is different for each line suggesting that different physical conditions might be present in different cloud structures. A slight change in CO morphology is apparent for the western region when comparing the ^{12}CO$(1-0)$, ^{12}CO$(2-1)$, and ^{13}CO$(1-0)$ line emission at 4.5" (Fig. 2) and 2.9" (Fig. 3) resolution: the small-scale geometry like the ridge connecting the peaks at a relative declination at +5" and 0" becomes more evident in the ^{12}CO$(1-0)$ and ^{13}CO$(1-0)$ maps. The difference is likely due to an extended low excitation component which is contributing more to the ^{12}CO$(1-0)$ line emission than the ^{12}CO$(2-1)$ one.

No significant offset is seen between the peaks in ^{12}CO$(1-0)$ and ^{13}CO$(1-0)$ (Fig. 5 and 6). We verified that the location of the peaks in the moment 0 maps is not significantly affected by the inclusion of the single dish data. Small offsets of a fraction of the beam are seen for some peaks (mainly in the ^{13}CO$(1-0)$ moment maps) as is expected in the case of low S/N data (being boosted by the additional signal from the single dish data). In addition, as the physical conditions across the spiral arms are changing as shown in §4, a

perfect one-to-one correspondence between the ^{12}CO$(1-0)$ and ^{13}CO$(1-0)$ morphology is not expected. The absence of an obvious shift is in apparent contradiction to the result of Tosaki et al. (2002) who found that the ^{13}CO$(1-0)$ emission is leading the ^{12}CO$(1-0)$ emission in particular in the southern region. One explanation could be that this apparent offset is caused more by an offset in the diffuse gas than in the more clumpy components which are better resolved with the OVRO data. Another possibility is the instrumental offset we had to correct for when aligning the single dish and interferometric data (see §2.2). As the offset is mainly in RA for the ^{12}CO$(1-0)$ single dish data this could explain the observed difference seen for the Western arm. If an instrumental effect is also causing the mismatch for the Southern arm, the astrometry of the ^{13}CO$(1-0)$ single dish data should be responsible.

The smooth ridges present in the ^{12}CO$(1-0)$ intensity map of Aalto et al. (1999) break up into smaller peaks at ∼1.6" resolution achieved in the ^{12}CO$(2-1)$ data. In particular the western region (Fig. 7) splits into two gas lanes over a length of about 10" (~ 410 pc) while the southern region (Fig. 8) shows up to three spurs along the leading side of the spiral arm similar to the features studied by Corder et al. (2008). The peaks in both regions appear to be slightly resolved at that resolution.

3.2. CO Kinematics

The 1.6" resolution ^{12}CO$(2-1)$ data allows us to study the molecular gas kinematics at about 65 pc resolution. Although the overall kinematics corresponds well with the low angular resolution velocities of (Aalto et al. 1999, their Fig. 3), the iso-velocities showing small deviations indicate that some GMC associations (GMAs) move faster or slower (fig. 7 middle). While the general deviations from a pure rotational disk are present as well indicating an overall non-circular component, some peaks stand out in the velocity dispersion map suggesting that a few peculiar velocities in the velocity maps are due to a superposition of GMCs rather than actual streaming motions. The most obvious example is the peculiar velocity field structure identified as streaming motion across the southern arm by Aalto et al. (1999) that is likely caused by a superposition of two GMCs rather than a distinct velocity feature due streaming (Fig. 8 middle and bottom). The high velocity dispersion observed in the GMA at offsets of +5" and +0" (GMA A10 following the nomenclature of Aalto et al. 1999) and the break-up into several sub-components of the GMA at offsets +12" and +2" (GMA A9) support our interpretation. In addition, the 1.6" resolution ^{12}CO$(2-1)$ data reveals that the higher velocity dispersion ridge seen in the ^{12}CO$(1-0)$ mosaic of Aalto et al. (1999) in particular in the western arm belongs to the second set of line peaks on the inner

side of the spiral arm (see Fig. 7 right).

3.3. Dense Gas Tracers

HCN(1-0) and HCO+(1-0) line emission was only detected in the western arm region at a low significance level (see Fig. 2). HCO+(1-0) is confined to the bright CO peak at about -2" and +0" while HCN(1-0) might be associated also with another bright CO peak north of this position. Given the low significance of the detection these data are not included in the following analysis.

4. Non-LTE Analysis

In order to estimate the physical conditions in the molecular gas along the gas spiral arm we measured the CO line emission in all four transitions for several positions along the spiral arms. As emission from the $C^{18}O(1-0)$ line was only detected in a small fraction of the positions, we will focus on the $^{12}CO(1-0)$, $^{12}CO(2-1)$, and $^{13}CO(1-0)$ line measurements for our analysis.

4.1. Line Ratios

14 and 9 positions were selected in the western arm region by basically centering them on distinct peaks of the CO line emission in the 2.9" and 4.5" resolution maps, respectively. In the southern region 7 positions were selected in a similar manner at 4.5" resolution only. The western 2.9" resolution and southern 4.5" resolution positions are indicated in Fig. 9 and 10, respectively. For the measurement of the line ratios R_{21} of the $^{12}CO(2-1)$ to $^{12}CO(1-0)$ line, R_{13} of the $^{12}CO(1-0)$ and $^{13}CO(1-0)$ line and R_{18} of the $^{12}CO(1-0)$ and $C^{18}O(1-0)$ line all data cubes were converted from flux density with units of Jy/beam to brightness temperature with units of K. For each position spectra of the four CO lines were extracted at the central pixel. In a few positions spectra showed evidence for two line components suggesting that more than one GMC is contributing to the emission peak. In these cases two Gaussians were fit to the spectra.

The integrated line fluxes were derived from Gaussian fits to the spectra and are listed in Tab. 5 and Tab. 6 for the 2.9" and 4.5" resolution data. Upper limits for the line flux were derived using three times the rms in the spectrum multiplied by the FWHM measured for the $^{12}CO(1-0)$ line. The listed line width corresponds to the FWHM of the $^{12}CO(1-0)$ line.

The line ratios R_{21}, R_{13} and R_{18} were derived by scaling the overall shape of the ^{12}CO$(2-1)$, ^{13}CO$(1-0)$ and C^{18}O$(1-0)$ spectra to the corresponding ^{12}CO$(1-0)$ spectrum and are listed in Tab. 5 and 6 as well. Thus the listed line ratios might not agree perfectly with a line ratio derived from the integrated line fluxes. This approach is more robust in the case of low S/N spectra than using the peak or integrated line flux which could be strongly effected by noise peaks. If no line was detectable in the data, we used the peak flux (upper limit) of the lines in question to derive a lower limit for the R_{13} and R_{18} ratios.

The derived line ratios R_{21} and R_{13} for the 2.9" resolution western and 4.5" resolution southern region are shown as a function of position in Fig. 9 and 10, respectively. In the western region the R_{21} ratio is basically monotonically decreasing as a function of galactocentric distance with a value of R_{21}=0.72 at position w1 corresponding to a radius of about 1.1 kpc ($\sim$ 27") and values between 0.42 and 0.47 for positions w11 to w14 which are at a radial distance of about 1.5 kpc ($\sim$ 37"). The R_{13} ratio on the other hand shows a spread of values between 4.5 (w14) and 7.5 (w5) with no clear radial trend. However, most of the higher values are found close to the area of brightest CO emission. While the western region covers a larger range in galactic radii, the southern region is basically tracing molecular gas located at roughly 2.6 kpc distance from the center. Thus the R_{21} and R_{13} have fairly similar values over most of the positions, except for the most eastern ones (S6 and S7) which are located close to a very large HII region (see §5) and show a double line profile. It is interesting to note that both regions exhibit one component where the ratios are slightly higher than those found for the southern most positions in the western region. We note that all trends seen within a single pointing should be real, as calibration uncertainties should only affect the absolute flux levels and thus all positions investigated in the same way.

4.2. LVG Parameters

To constrain the physical conditions of the GMCs we use an spherical, isothermal one-component large velocity gradient (LVG) model (Scoville & Solomon 1974; Goldreich & Kwan 1974). This treatment of the radiative transfer is valid for clouds in which a large-scale velocity gradient effectively makes the radiative transfer a local problem not requiring self-consistent solutions for the entire cloud. The assumption for this model is that due to the velocity gradient present the emission of a molecule is Doppler-shifted with respect to molecules in the rest of the cloud. For the models presented here we fixed the ^{12}CO abundance relative to H_2 and the ^{12}CO/^{13}CO abundance ratio to 8.0e-5 and 30, respectively. The numbers correspond to values found in GMCs in the inner 3 kpc of the disk of the Milky Way (e.g. Langer & Penzias 1993; Milam et al. 2005). LVG models were calculated for two

different assumption on the velocity gradient: a) a fixed value of $\frac{\mathrm{d}v}{\mathrm{d}r}$ set to $1\,\mathrm{km\,s^{-1}pc^{-1}}$ typically for local clouds and reasonable for M51's clouds[2], b) assuming a virialized cloud such that $\frac{\mathrm{d}v}{\mathrm{d}r} = 3.1\sqrt{\frac{n(H_2)}{10^4}}$ (e.g. Goldsmith 2001). LVG line intensity ratios were computed for kinetic gas temperatures $\mathrm{T_{kin}}$ between 3 and 200 K and $\mathrm{H_2}$ densities $\log n(\mathrm{H_2})$ between 2.0 and 4.0 (for details of the model, see Weiß et al. 2001).

4.3. M51 model results

The results of the LVG analysis are presented in Fig. 9 and 10 and summarized in Tab. 7. Typical relative errors on the derived temperature are of the order of (75-100)% implying that solutions preferring higher temperatures are in principle also consistent with the low temperatures found for several locations. For the $\mathrm{H_2}$ densities of $N(\mathrm{H_2})$ and $n(\mathrm{H_2})$ we find typical relative errors of about 25% (going up to ∼50% in the less constrained cases). These errors are independent on the assumptions made for the velocity gradient.

The bulk of the CO emission probed here arises from cold clouds ($\mathrm{T}_{kin} \sim$ 16-20 K, depending on the assumption made for the velocity gradient) with moderate $\mathrm{H_2}$ density of $n(\mathrm{H_2}) \approx 240 - 120\,\mathrm{cm^{-3}}$. It is interesting to note that the $\mathrm{H_2}$ density in the assumption of a virialized cloud is typically (50-65)% of the $\mathrm{H_2}$ density derived for a fixed velocity gradient. The average conversion factor derived from the LVG analysis of $X_{CO} = (1.3-2.0)\times 10^{20}\,\mathrm{cm^{-2}K^{-1}km^{-1}s}$ is close to the Galactic value[3] of $X_{CO} = (1.8\pm0.3)\times10^{20}\,\mathrm{cm^{-2}K^{-1}km^{-1}s}$. This value was recently derived for the Milky Way by Dame et al. (2001) suggesting that the GMCs analyzed here are similar to those in the Milky Way, especially when assuming that they are all virialized clouds. Thus the data presented here mainly probe the diffuse component of the ISM and not the dense gas that is involved in current star formation. In the remainder we refer to the LVG results assuming virialized clouds. However, all trends discussed are present in both scenarios.

The most obvious spatial variation of the gas physical condition is a decrease of the kinetic temperature with increasing galacto-centric radius along the western spiral arm region. Temperatures decrease from about 27 K at 1.1 kpc (position w1) to <10 K at 1.6 kpc (position w14). This might indicate an effect of the interstellar radiation field (ISRF) on the cloud properties as these radii probe the transition from the central (bulge) region into the

[2]For an average line width of $40\,\mathrm{km\,s^{-1}}$ (see e.g. Tab. 5) and an average cloud complex size of ∼50 pc (see §5).

[3]First determined by Sanders et al. (1984).

disk (for a discussion of the effect of HII regions see §5). In the southern region, with an almost constant galacto-centric radius of ~ 2.6 kpc, no such gradient is detected. These more distant regions are on average 5-10 K warmer than the furthest regions in the Western arm (position w12 and w14). The derived radial temperature profile by Meijerink et al. (2005) used to model the heating mechanism at 850μm shows a continuous decline of temperature with radius, however, the change over the distances relevant here is less than 2 K. The dust temperature map of Benford & Staguhn (2008) derived by fitting a grey-body thermal emission spectrum to data at 70, 160, 350 and 850 μm shows also an enhanced dust temperature at the center with a decline for larger radii. However, the dust temperature in the spiral arms themselves is higher than in the interarm regions. Overall the change in temperature is not dramatic. Benford & Staguhn (2008) report a mean temperature of (25±3) K for the disk while the inner 3 kpc region has a higher temperature of 31 K. Therefore it appears that more local changes (i.e. within the spiral arm) of the ISRF than the global radial trend could be causing the apparent observed trend in the Western arm. However, higher resolution data such as observations from the Herschel Space Observatory and subsequent detailed modeling are required to address this in more detail.

There is no obvious large difference in the temperature and H_2 density of GMCs close to or around star forming regions as traced by the presence of Hα emission (see §5, also indicated in Tab. 7). This finding suggests that the CO emission arising from or close to star-forming regions is still dominated by cold gas that is surrounding the HII regions and not immediately affected by the enhanced radiation from the HII region. There might be a slight effect present as half of the positions in the Southern arm encompass HII regions (traced by Hα emission) and show slightly higher temperatures. The impact of star formation on the molecular clouds (e.g. heating at the cloud surfaces) is not measurable at a linear resolution of 180 pc (or even for the higher 120 pc resolution data). Only two positions stand clearly out: w5 in the western region and S7(B) in the southern region that show the highest kinetic temperature of $T_{kin} = 50$ K, average H_2 densities and the lowest conversion factor of $X_{CO} = 0.5(0.8) \times 10^{20}\,\mathrm{cm^{-2}K^{-1}km^{-1}s}$. Both GMC complexes are located on the inner edge of the CO spiral arm suggesting that they either live in a different environment than the clouds studied in the other locations or that their ISM has been heavily affected by the ongoing neighboring massive star formation [in the case of S7(B)].

4.4. X_{CO} measurements for M51

Several studies were conducted in the past to derive the conversion factor X_{CO} for the molecular gas in M51. Most of these studies did find values well below a Galactic value of

$X_{CO} = (1.8 \pm 0.3) \times 10^{20}\,\mathrm{cm^{-2}K^{-1}km^{-1}s}$ (Dame et al. 2001). Several reasons could explain the apparent mismatch between our results and these earlier works. One main advantage of the work presented here is its superior spatial resolution compared to the previous results.

Using single dish observations of ^{12}CO and ^{13}CO line transitions and three different methods Garcia-Burillo et al. (1993) find a value of $X_{CO} = (0.8 \pm 0.3) \times 10^{20}\,\mathrm{cm^{-2}K^{-1}km^{-1}s}$ for the center and the molecular spiral arms from LVG modeling and an even lower value when using only the ^{13}CO emission line data. Assuming a constant ratio between the extinction and the H_2 column density $N(H_2)$ as found for our Galaxy (Bohlin et al. 1978) gave a Galactic value of $X_{CO} \sim 1.8 \times 10^{20}\,\mathrm{cm^{-2}K^{-1}km^{-1}s}$. Extending this work Guelin et al. (1995) added 1mm continuum measurements to estimate X_{CO} via the gas-to-dust ratio, again getting factors about 4 times lower than the standard value. The most likely explanation for the mismatch is that in these studies individual GMC complexes are not resolved and thus a significant mixing of vastly different cloud properties can happen.

Using interferometric observations of the molecular gas disk Nakai & Kuno (1995) applied the A_V method[4] to those HII regions in the spiral arms that had both Hα as well as radio continuum emission (van der Hulst et al. 1988) that allowed for a good extinction estimate. They obtained a value of $X_{CO} \sim (0.9 \pm 0.1) \times 10^{20}\,\mathrm{cm^{-2}K^{-1}km^{-1}s}$ at about 10" resolution. Among possible sources of error they list a bias for probing gas with higher excitation temperatures as they are looking toward HII region where the gas could be potentially more heated. They also caution that the conversion factor in the inter-arms might be completely different as the conditions for the molecular gas are expected to vary as well. Given that most of the gas for which we derived the conversion factor is not close to HII regions (see §5) those measurements are very likely affected by probing a very different environment than we did.

Interestingly, applying virial mass measurements to the GMAs in the spiral arms of M51, Rand & Kulkarni (1990) and Adler et al. (1992) come to very opposite conclusions of $X_{CO} \sim 3 \times 10^{20}\,\mathrm{cm^{-2}K^{-1}km^{-1}s}$ and $X_{CO} \sim 1.2 \times 10^{20}\,\mathrm{cm^{-2}K^{-1}km^{-1}s}$, respectively. Both studies measure virial masses assuming that the GMAs are resolved with typical sizes of 300-400 pc. In order to apply this method the assumption must be that the GMAs are bound complexes which might not be true given the fact that it is unclear whether they are just a gas accumulation due to orbit crowding or indeed self-gravitating entities (e.g. Rand & Kulkarni 1990; Adler et al. 1992). This is still an open issue discussed by Koda et al. (2009) for the GMAs identified in their high fidelity map as the elongated structure could easily be

[4]The adopted method by Nakai & Kuno (1995) takes into account gas located behind HII regions on a statistically basis.

interpreted as being due to orbit crowding rather than resembling a bound entity even at their 4" resolution. As our high resolution ^{12}CO$(2-1)$ data shows that these GMAs break up into several clumps that might no longer even correspond to a single gas lanes (as e.g. seen in the Western region), it seems sensible that the assumption of bound systems is not valid for all GMAs. In addition, enhanced velocity dispersion due to shocks or streaming motions will critically affect the measurements of the line width at the 10" resolution of the data used by the previous studies. Since Adler et al. (1992) mainly analyzed GMAs located in the central region where the dynamical properties are changing faster, this could be a possible explanation for the different results of both works as the method used is basically the same.

Taking a different approach and combining measurements of the first three transitions of ^{12}CO with those of ISM cooling lines, Kramer et al. (2005) used a PDR (photon-dominated region) model. However, their derived densities for the center and two regions covering the spiral arms at slightly larger radii are about 1 order of magnitude higher while their temperatures of 12.5 and 15 K are similar to our findings. A recent similar study of the central 3.5 kpc using a refined PDR model by Bell et al. (2007) finds a X_{CO} of 1/10 the Galactic value. As both studies were also done at low resolution, it is not clear that the ISM cooling lines as well as the CO lines have the same distribution and filling factors which could affect the estimation of X_{CO}. Given that the molecular gas studied here is clearly not located closely to HII regions, it is it not obvious that the PDR assumption is applicable for our regions (see §5).

Since it is expected that X_{CO} is changing as a function of environment, the assumption of a single excitation and a simple geometry over a large region can frequently yield misleading results. As our measurements have the highest spatial resolution and are confined to mainly probing a single environment, they should present a good estimate of X_{CO} for the spiral arms probed. Given the large uncertainties involved when averaging over large areas in a galaxies, they are consistent with the previous results and only highlight the fact that deriving an average X_{CO} for an entire galaxy is not straight-forward. In particular the relation between the conversion factor and the gas density and temperature $X_{CO} \sim \mathrm{T}_{\mathrm{kin}}^{-1}\mathrm{n}(\mathrm{H}_2)^{0.5}$ can explain why the conversion factor is lower for studies that include a large fraction of the (presumably) less dense inter-arm gas.

4.5. Comparison to GMCs in other spiral galaxies

The LVG models suggest that the physical conditions in the GMCs in the spiral arms of M 51 are very similar to those in the Milky Way which have typical gas temperatures

and densities of 10 K and above 200 cm^{-3}, respectively (e.g. Scoville & Sanders 1987) (for a recent compilation see Tielens 2005). Also the observed average H_2 column density in M51's GMCs of $N(H_2) = (2.3 - 3.2) \times 10^{22}\,cm^{-2}$ is similar to that typically found for GMCs in the Galactic plane of $N(H_2) \sim 4{\times}10^{22}\,cm^{-2}$ (Solomon et al. 1979).

Studies of GMCs in local group galaxies found that the cloud properties do vary between clouds with and without the presence of star formation. Wilson et al. (1997) analyzed seven GMCs in M33 at 22" resolution (corresponding to roughly 90 pc) using multi-line CO observations in conjunction with a LVG model. They find that GMCs without star formation are typically colder with $T_{kin} \sim 10 - 20$ K than GMCs with star formation present showing $T_{kin} \sim 30 - 100$ K for our assumed $[^{12}CO]/[^{13}CO]$ abundance ratio of 30. While the temperatures for the cold GMC population is similar to our values for M51, their derived densities are about 1 order of magnitude higher than our estimates for M51. Interestingly, they note that the sphere of influence for HII regions seems limited as GMCs within 120 pc distance of an HII region do already show normal properties and no effect of heating. A recent study of GMCs in the Large Magellanic Cloud by Minamidani et al. (2008) also find a correlation between the star formation activity (measured by the Hα flux) and the temperature and density of the GMCs themselves. They propose an evolutionary sequence from cool ($T_{kin} \sim 10 - 30$ K) and low density ($\log(n(H_2)) < 3$) GMCs, through warm ($T_{kin} \sim 30$ - 200 K) and cool low density GMCs to warm and dense GMCs where the first two types are in a young star formation phase where density has not yet reached high enough values to cause active massive star formation. GMCs in the last category are in a later star formation phase where the average density is higher.

Thus we conclude that the bulk of the GMCs observed in M51's spiral arms are very similar to the ones in our own Galaxy and given their low temperatures are likely not impacted by (ongoing) star formation. This is not that surprising as most HII regions are located close to CO peaks but rarely do coincide (see §5) and as suggested by the M33 results from Wilson et al. (1997) the sphere of influence of an HII region is small. This could also suggest that GMCs located in spiral arms are different from GMCs located in the center of starburst galaxies such as M82. Weiß et al. (2001) found significantly higher kinetic temperatures of T_{kin} between 50 and 190 K as well as gas densities ($n(H_2)$ between $5{\times}10^2$ and $2{\times}10^4\,cm^{-3}$) and concluded that the ongoing massive star formation is significantly altering the cloud properties.

5. The Relation of the Molecular ISM to Sites of Star Formation

In order to compare the distribution of the molecular gas with the sites of recent star formation we use our CO data and archival HST images from Scoville et al. (2001). As expected the molecular gas coincides very well with the prominent dust lanes seen in the individual spiral arms. Using the 1.6" resolution ^{12}CO$(2-1)$ data one can see that the emission peaks do fall into regions of high extinction obvious in the HST V band image (Fig. 11 and 12). In particular, the double gas lane in the brightest part of the western region does show a line of enhanced V band emission between the two CO lanes.

While enhanced extinction is present across the full width of the gas spiral arms of $\sim$ 7" it is not uniform but rather patchy. The widths of the dust lanes visible in the HST V band image range from about 0.5" to 2" suggesting that the GMCs we resolve in the ^{12}CO$(2-1)$ data are causing the extinction and that the molecular gas is mainly distributed within GMCs. An upper limit on the scale height of the gas disk is about 20–80 pc if we assume that the extincting material can not have a larger vertical extent than a dust lane is wide. Combining these numbers with the derived H_2 column densities N(H_2) in §4 (see Tab. 7) returns approximately the H_2 volume densities n(H_2) obtained by the LVG analysis. This implies that most of the GMCs seen at 1.6" resolution are mostly single entities and not blends of several GMCs.

Most of the HII regions as traced by their Hα and Paα line emission lie downstream of the molecular gas as it is expected if star formation is occurring inside the molecular gas spiral arms (see Fig. 11 and 12). Since the southern region is closer to corotation (where the pattern speed is closer to the angular velocity) than the western region, this can explain why two of the ^{12}CO$(2-1)$ peaks coincide with star formation whereas only one does so in the western region. Except for one case, all Paα peaks have Hα emission associated with them suggesting that extinction is not extreme towards HII regions.

It is interesting to compare the average extinction toward HII regions derived from the recombination line ratios of Hα and Paα of $A_V \sim 3.0$ (Scoville et al. 2001) with those estimated from the CO data. We use equation (6) from Nakai & Kuno (1995) of $N(H_2) = 1.87 \times 10^{21}\, A_V\, [mag] - N(HI)[cm^{-2}]/2$ and our average H_2 column density of $< N(H_2) >= (2.3-3.3) \times 10^{22}\,\mathrm{cm}^{-2}$. Since the ISM is mostly molecular in the regions studied here, e.g. Schuster et al. (2007) find values for the ratio of surface density of $\sum_{HI} / \sum_{H_2} < 0.2$ for r$\leq$ 1.6 kpc and $\sim$ 0.5 for the southern region at 2.6 kpc, we neglect the contribution from atomic hydrogen. The derived extinction is about $A_V \sim 12-18$, significantly larger than that measured in the HII regions. This value is even larger ($A_V \sim (15-33)$) then using a Galactic relation of $N(H_2)/A_V = 10^{21}\, cm^{-2} K^{-1} s$ (Bohlin et al. 1978). Thus a lot of massive star formation could be hidden inside the gas spiral arms and only be detectable at longer

wavelengths such as the infrared and radio. Using the HiRes deconvolved 24 μm MIPS image (Dumas et al., subm.) and the Hα map from Calzetti et al. (2005) we tested this scenario at 2" resolution. As the 24μm emission coincides with the CO emission and is thus mainly arising inside (or upstream) the Hα emission (see Fig. 11 and 12), this supports the picture that hidden star formation does occur inside the spiral arms. Using the Hα emission located in the spiral arms and 24μm emission arising from the same area, star formation rates (SFRs) can be estimated[5]. Correcting the observed Hα flux for the average extinction of $A_V \sim 3$ found for HII regions (Scoville et al. 2001) and using the SFR prescriptions of Kennicutt (1998) for Hα and of Rieke et al. (2009) for the 24 μm data, we find that the SFR hidden in the spiral arms is about 50% of that traced by Hα. This 'lack' of (embedded) star formation inside the gas spiral arms is consistent with the fact that the molecular gas is still cold and might therefore have not yet started to form new stars.

There is no strong correlation between the location of bright HII regions and massive CO clouds or holes, though most HII regions tend to lie next to a ^{12}CO$(2-1)$ peak. This would be in line with the picture described by Bastian et al. (2005) who found a correlation between the radius and mass for clusters of star clusters that is similar to the relation seen for GMCs. They interpret this as evidence that a GMC does form an assemble of star clusters.

6. The impact of the star formation on the ISM

The physical properties of the GMC complexes located in the spiral arms of M 51 are very similar to those observed for GMCs in our Galaxy. Our LVG analysis suggests that the conversion factor between CO line emission and H_2 mass is similar to the standard conversion factor X_{CO}. This result is in apparent contradiction to other studies conducted in M 51 at significantly lower angular resolution. The simplest explanation is that the conversion factor is not constant across the disk (or even within the spiral arms) but a function of environment (even for the diffuse gas probed here). Therefore a spatial resolution matched to the size of GMC complexes is required to obtain reasonable numbers. Further, the assumption of a single value is not correct when measuring the total amount of gas present in a nearby spiral galaxy. Our 65 pc resolution ^{12}CO$(2-1)$ data shows that the spiral arms break up into clumps at these scales that are roughly aligned along the spiral arms. In the western region the CO peaks are more abundant toward the leading side of the spiral showing a slight shift from the peak of the more smooth emission as traced by, e.g., the 4.5" resolution ^{12}CO$(1-0)$

[5]We do not subtract the contribution from the diffuse emission as star formation appears to be the dominant source for the Hα and 24μm emission in the spiral arms.

emission (see Fig. 2 and 7). No offset is obvious for the southern region (see Fig. 4 and 8) as expected as the pattern is moving close to the angular velocity at these radii.

At our 120 pc resolution we find no evidence that star formation in HII regions is impacting the properties of the GMCs that are at about ≥1" (40 pc) distance, in agreement with findings in M33 by Wilson et al. (1997). Only two positions which are located at the inner edge of the spiral arm exhibit elevated temperatures that may be related to the large-scale dynamics.

Based on the observations presented here, we conclude that most of the GMCs in the spiral arms of M51 are cold, dense structures that are not heavily affected by the neighboring star forming HII regions. Despite the inferred high extinction of $A_V \sim (15 - 30)$ towards these GMCs only about 50% of the star formation traced by Hα emission is coinciding with the gas spiral arms indicating that most of the molecular gas seen is not yet actively forming stars.

7. Summary and Conclusions

M 51 offers the ideal environment to study the physical properties of the molecular gas in the spiral arms of a disk galaxy. Combining short spacing corrected interferometric observations of the ^{12}CO(1−0), ^{12}CO(2−1), and ^{13}CO(1−0) line emission in two selected arm regions in the central 6 kpc, a LVG analysis finds that the GMCs inside the spiral are similar to those observed in our Galaxy. The average kinetic temperature and H_2 density (assuming virialized clouds) are $T_{kin} = 20$ K and $n(H_2) = 120\,cm^{-3}$, respectively, at a linear resolution of 120 pc (290 pc for the southern region). Similarly, the derived conversion factor X_{CO} is close to the Galactic value of $1.8 \times 10^{20}\,cm^{-2}K^{-1}\,km^{-1}s$ recently derived by Dame et al. (2001). We interpret our results such that the physical properties of the GMC population do not change much as a function of environment in galaxy disks, consistent with the findings of Bolatto et al. (2008) who analyzed GMC properties in local galaxies.

Comparison of the derived molecular gas properties to the location of star formation shows no obvious trend suggesting that the massive star formation has no strong impact onto the GMCs inside the spiral arms. Comparison of the extinction inferred from the derived H_2 density and measured toward HII regions shows that the extinction toward the molecular clouds is at least a factor of 5 higher with an average A_V of 15–30 mag than the average A_V of 3.1 inferred for HII regions by Scoville et al. (2001).

Based on observations carried out with the IRAM 30m telescope. IRAM is supported by

INSU/CNRS (France), MPG (Germany) and IGN (Spain). We thank very much K. Schuster and C. Kramer for making available to us the HERA $^{12}CO(2-1)$ data cube and G. Dumas for the HiRes version of the MIPS 24μm image as well as her help with the SFRs. We are thankful for the public access to the 'Nobeyama CO Atlas of Nearby Spiral Galaxies'. The comments and suggestions by the anonymous referee were highly appreciated and helped to improve the paper. The Owens Valley Radio Observatory was funded in part by NSF grant AST 99-81546.

OVRO, IRAM (30m)

REFERENCES

Aalto, S., Hüttemeister, S., Scoville, N. Z., & Thaddeus, P. 1999, ApJ, 522, 165

Adler, D. S., Lo, K. Y., Wright, M. C. H., Rydbeck, G., Plante, R. L., & Allen, R. J. 1992, ApJ, 392, 497

Bastian, N., Gieles, M., Efremov, Y. N., & Lamers, H. J. G. L. M. 2005, A&A, 443, 79

Bell, T. A., Whyatt, W., Viti, S., & Redman, M. P. 2007, MNRAS, 382, 1139

Benford, D. J., & Staguhn, J. G. 2008, in Astronomical Society of the Pacific Conference Series, Vol. 381, Infrared Diagnostics of Galaxy Evolution, ed. R.-R. Chary, H. I. Teplitz, & K. Sheth, 132–+

Bohlin, R. C., Savage, B. D., & Drake, J. F. 1978, ApJ, 224, 132

Bolatto, A. D., Leroy, A. K., Rosolowsky, E., Walter, F., & Blitz, L. 2008, ApJ, 686, 948

Calzetti, D., Kennicutt, Jr., R. C., Bianchi, L., Thilker, D. A., Dale, D. A., Engelbracht, C. W., Leitherer, C., Meyer, M. J., Sosey, M. L., Mutchler, M., Regan, M. W., Thornley, M. D., Armus, L., Bendo, G. J., Boissier, S., Boselli, A., Draine, B. T., Gordon, K. D., Helou, G., Hollenbach, D. J., Kewley, L., Madore, B. F., Martin, D. C., Murphy, E. J., Rieke, G. H., Rieke, M. J., Roussel, H., Sheth, K., Smith, J. D., Walter, F., White, B. A., Yi, S., Scoville, N. Z., Polletta, M., & Lindler, D. 2005, ApJ, 633, 871

Corder, S., Sheth, K., Scoville, N. Z., Koda, J., Vogel, S. N., & Ostriker, E. 2008, ApJ, 689, 148

Dame, T. M., Hartmann, D., & Thaddeus, P. 2001, ApJ, 547, 792

Feldmeier, J. J., Ciardullo, R., & Jacoby, G. H. 1997, ApJ, 479, 231

Garcia-Burillo, S., Guelin, M., & Cernicharo, J. 1993, A&A, 274, 123

Goldreich, P., & Kwan, J. 1974, ApJ, 189, 441

Goldsmith, P. F. 2001, ApJ, 557, 736

Guelin, M., Zylka, R., Mezger, P. G., Haslam, C. G. T., & Kreysa, E. 1995, A&A, 298, L29+

Kennicutt, Jr., R. C. 1998, ARA&A, 36, 189

Koda, J., Scoville, N., Sawada, T., La Vigne, M. A., Vogel, S. N., Potts, A. E., Carpenter, J. M., Corder, S. A., Wright, M. C. H., White, S. M., Zauderer, B. A., Patience, J., Sargent, A. I., Bock, D. C. J., Hawkins, D., Hodges, M., Kemball, A., Lamb, J. W., Plambeck, R. L., Pound, M. W., Scott, S. L., Teuben, P., & Woody, D. P. 2009, ApJ, 700, L132

Kramer, C., Mookerjea, B., Bayet, E., Garcia-Burillo, S., Gerin, M., Israel, F. P., Stutzki, J., & Wouterloot, J. G. A. 2005, A&A, 441, 961

Langer, W. D., & Penzias, A. A. 1993, ApJ, 408, 539

Lee, M. G., Chandar, R., & Whitmore, B. C. 2005, AJ, 130, 2128

Meier, D. S., & Turner, J. L. 2001, ApJ, 551, 687

Meier, D. S., Turner, J. L., & Hurt, R. L. 2008, ApJ, 675, 281

Meijerink, R., Tilanus, R. P. J., Dullemond, C. P., Israel, F. P., & van der Werf, P. P. 2005, A&A, 430, 427

Milam, S. N., Savage, C., Brewster, M. A., Ziurys, L. M., & Wyckoff, S. 2005, ApJ, 634, 1126

Minamidani, T., Mizuno, N., Mizuno, Y., Kawamura, A., Onishi, T., Hasegawa, T., Tatematsu, K., Ikeda, M., Moriguchi, Y., Yamaguchi, N., Ott, J., Wong, T., Muller, E., Pineda, J. L., Hughes, A., Staveley-Smith, L., Klein, U., Mizuno, A., Nikolić, S., Booth, R. S., Heikkilä, A., Nyman, L.-Å., Lerner, M., Garay, G., Kim, S., Fujishita, M., Kawase, T., Rubio, M., & Fukui, Y. 2008, ApJS, 175, 485

Nakai, N., & Kuno, N. 1995, PASJ, 47, 761

Nakai, N., Kuno, N., Handa, T., & Sofue, Y. 1994, PASJ, 46, 527

Rand, R. J., & Kulkarni, S. R. 1990, ApJ, 349, L43

Rieke, G. H., Alonso-Herrero, A., Weiner, B. J., Pérez-González, P. G., Blaylock, M., Donley, J. L., & Marcillac, D. 2009, ApJ, 692, 556

Roberts, Jr., W. W., & Stewart, G. R. 1987, ApJ, 314, 10

Sanders, D. B., Solomon, P. M., & Scoville, N. Z. 1984, ApJ, 276, 182

Sault, R. J., Teuben, P. J., & Wright, M. C. H. 1995, in Astronomical Society of the Pacific Conference Series, Vol. 77, Astronomical Data Analysis Software and Systems IV, ed. R. A. Shaw, H. E. Payne, & J. J. E. Hayes, 433–+

Scheepmaker, R. A., Lamers, H. J. G. L. M., Anders, P., & Larsen, S. S. 2009, A&A, 494, 81

Schuster, K. F., Kramer, C., Hitschfeld, M., Garcia-Burillo, S., & Mookerjea, B. 2007, A&A, 461, 143

Scoville, N., Carlstrom, J., Padin, S., Sargent, A., Scott, S., & Woody, D. 1994, in Astronomical Society of the Pacific Conference Series, Vol. 59, IAU Colloq. 140: Astronomy with Millimeter and Submillimeter Wave Interferometry, ed. M. Ishiguro & J. Welch, 10–+

Scoville, N., & Young, J. S. 1983, ApJ, 265, 148

Scoville, N. Z., Polletta, M., Ewald, S., Stolovy, S. R., Thompson, R., & Rieke, M. 2001, AJ, 122, 3017

Scoville, N. Z., & Sanders, D. B. 1987, in Astrophysics and Space Science Library, Vol. 134, Interstellar Processes, ed. D. J. Hollenbach & H. A. Thronson Jr., 21–50

Scoville, N. Z., & Solomon, P. M. 1974, ApJ, 187, L67+

Shetty, R., Vogel, S. N., Ostriker, E. C., & Teuben, P. J. 2007, ApJ, 665, 1138

Solomon, P. M., Sanders, D. B., & Scoville, N. Z. 1979, ApJ, 232, L89

Tielens, A. G. G. M. 2005, The Physics and Chemistry of the Interstellar Medium, ed. A. G. G. M. Tielens

Tosaki, T., Hasegawa, T., Shioya, Y., Kuno, N., & Matsushita, S. 2002, PASJ, 54, 209

van der Hulst, J. M., Kennicutt, R. C., Crane, P. C., & Rots, A. H. 1988, A&A, 195, 38

Weiß, A., Neininger, N., Hüttemeister, S., & Klein, U. 2001, A&A, 365, 571

Wilson, C. D., Walker, C. E., & Thornley, M. D. 1997, ApJ, 483, 210

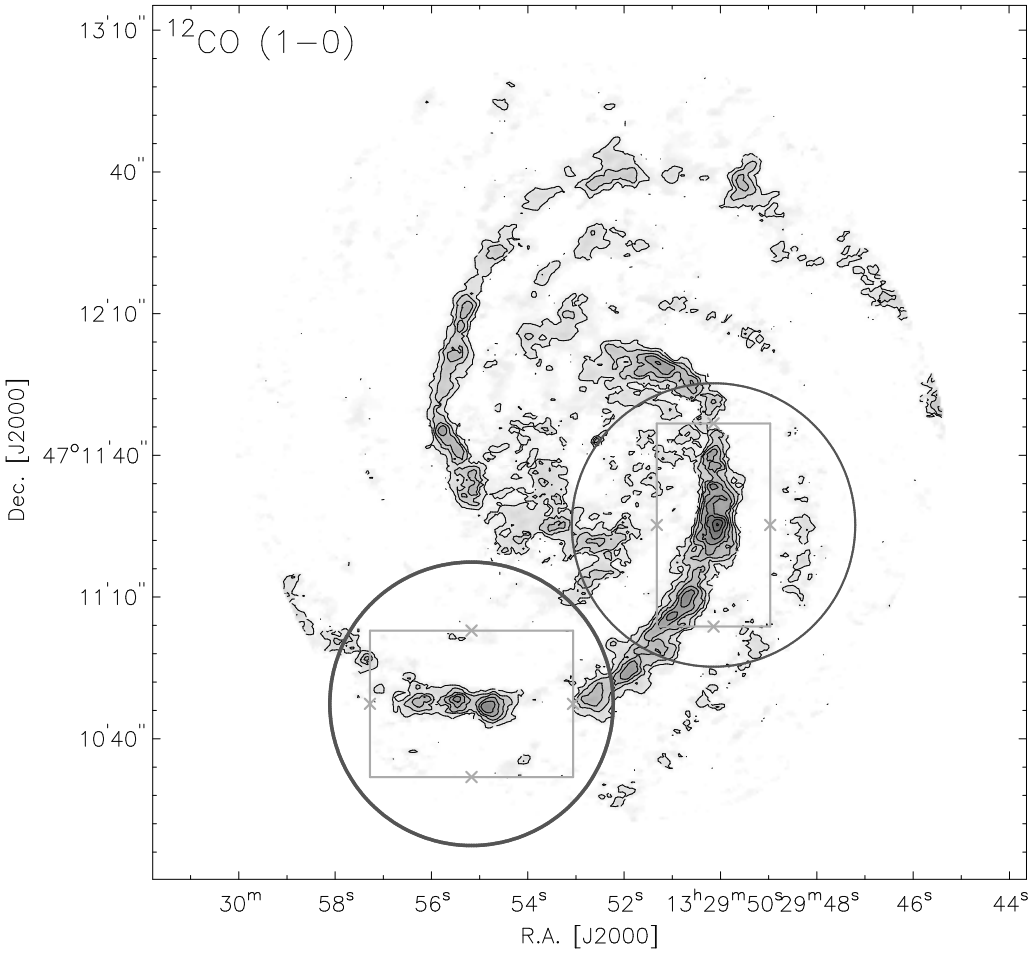

Fig. 1.— Location of the two OVRO pointings (dark circles) overlaid onto the integrated ^{12}CO(1-0) line emission (contours) from Aalto et al. (1999) with short spacing correction (SSC) applied. The size of the circles corresponds to the primary beam at 3mm. The light gray rectangles outline the western (top) and southern region (bottom) that are studied.

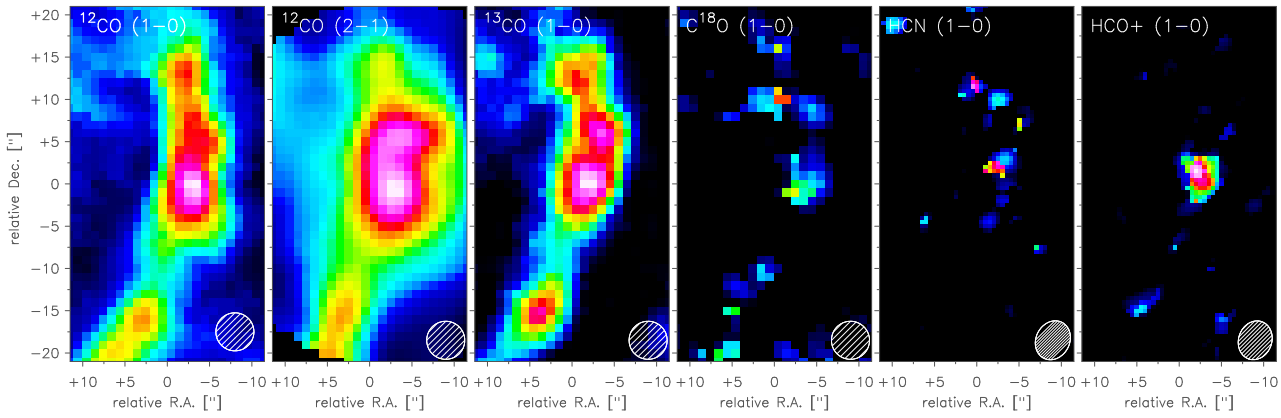

Fig. 2.— The western region at 4.5" resolution in molecular line emission of (from left to right): ^{12}CO$(1-0)$, ^{12}CO$(2-1)$, ^{13}CO$(1-0)$, C^{18}O (1-0), HCN (1-0), and HCO+(1-0). All maps shown are made from the SSC data cubes. The beam is shown in the bottom right corner of each panel. The angular offset is relative to the pointing center.

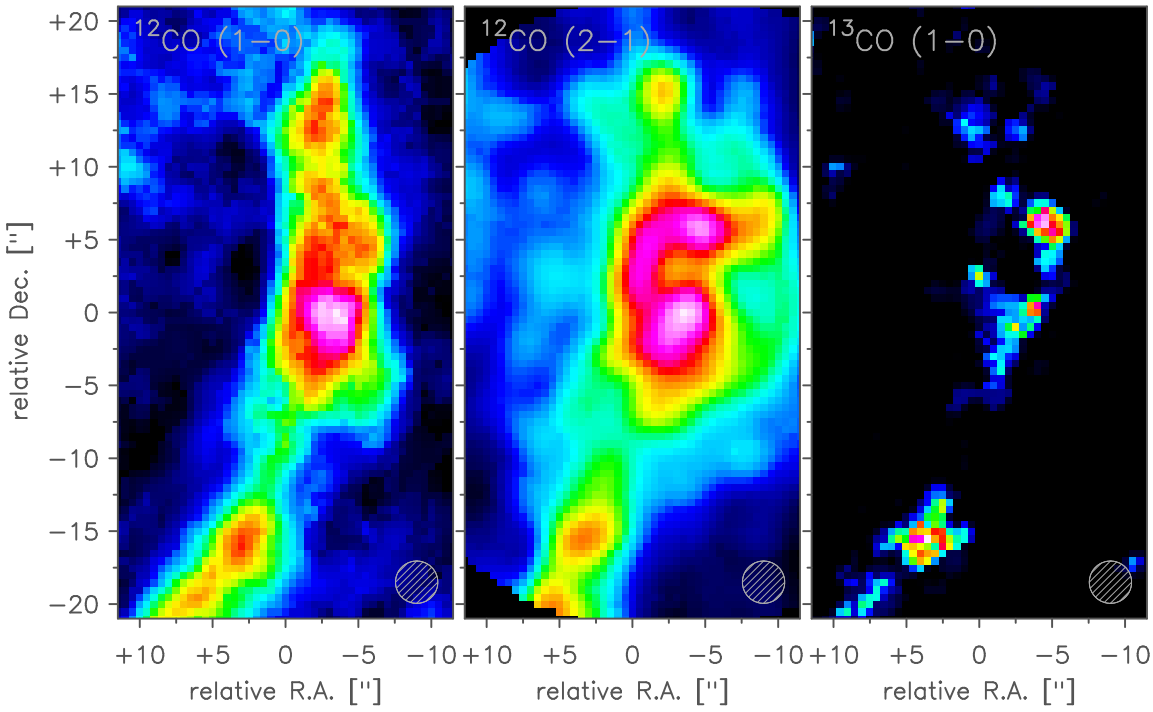

Fig. 3.— The western region at 2.9" resolution in molecular line emission of ^{12}CO$(1-0)$ (*left*), ^{12}CO$(2-1)$ (*middle*), and ^{13}CO$(1-0)$ (*right*). All maps shown are made from the SSC data cubes. The beam is shown in the bottom right corner of each panel. The angular offset is relative to the pointing center.

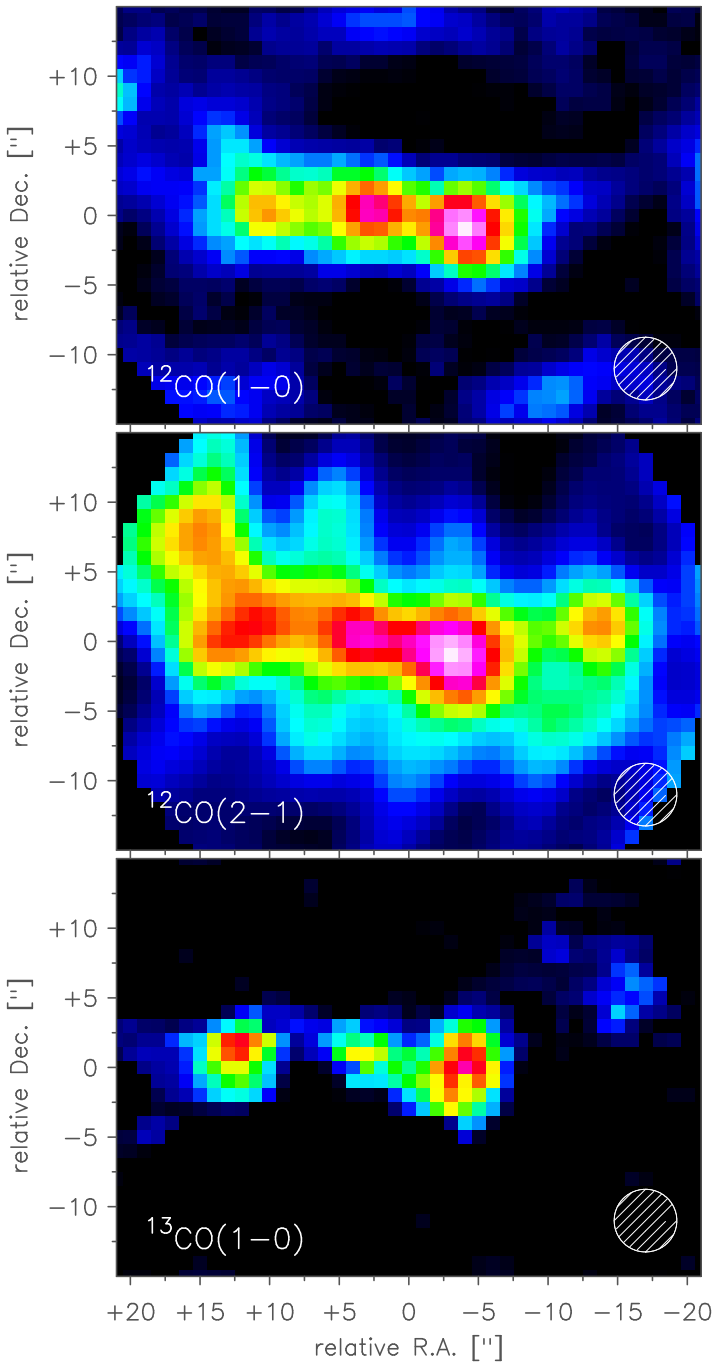

Fig. 4.— The southern region at 4.5" resolution in molecular line emission of $^{12}CO(1-0)$ (*top*), $^{12}CO(2-1)$ (*middle*), and $^{13}CO(1-0)$ (*bottom*). All maps shown are made from the SSC data cubes. The beam is shown in the bottom right corner of each panel. The angular offset is relative to the pointing center.

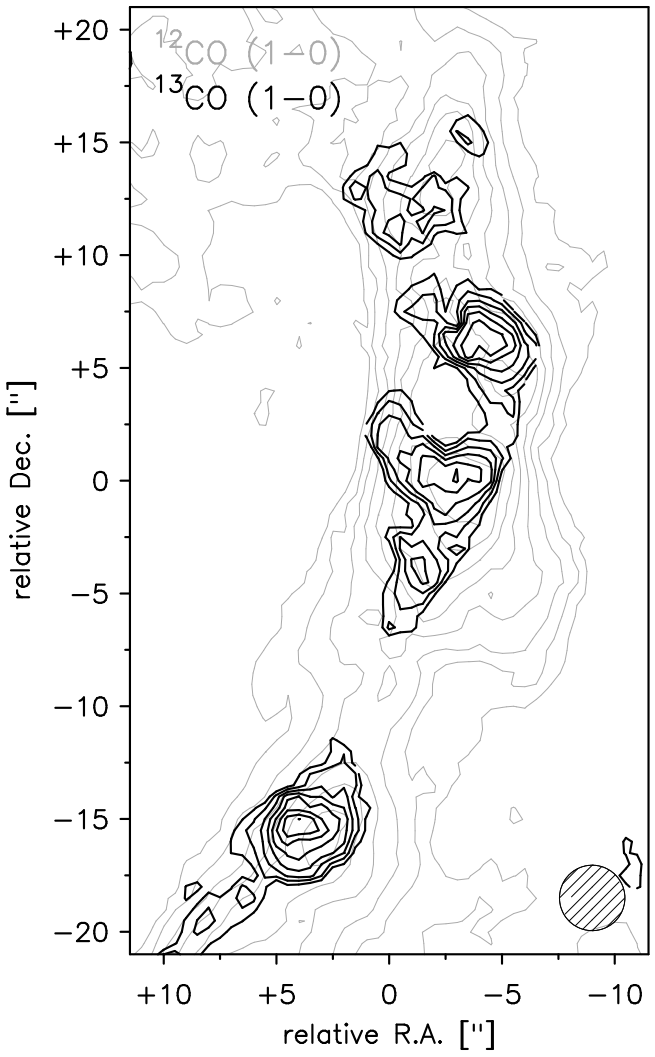

Fig. 5.— Comparison of the location of the peak emission in the ^{12}CO$(1-0)$ (gray contours) and ^{13}CO$(1-0)$ (black contours) in the western arm at 2.9" resolution. The contours are in steps of 10% of the maximum value of 295 K km s^{-1} starting at 20% for the ^{12}CO$(1-0)$ map and in steps of 10% of the maximum value of 37.3 K km s^{-1} starting at 30% for the ^{13}CO$(1-0)$ data. All maps shown are made from the SSC data cubes.

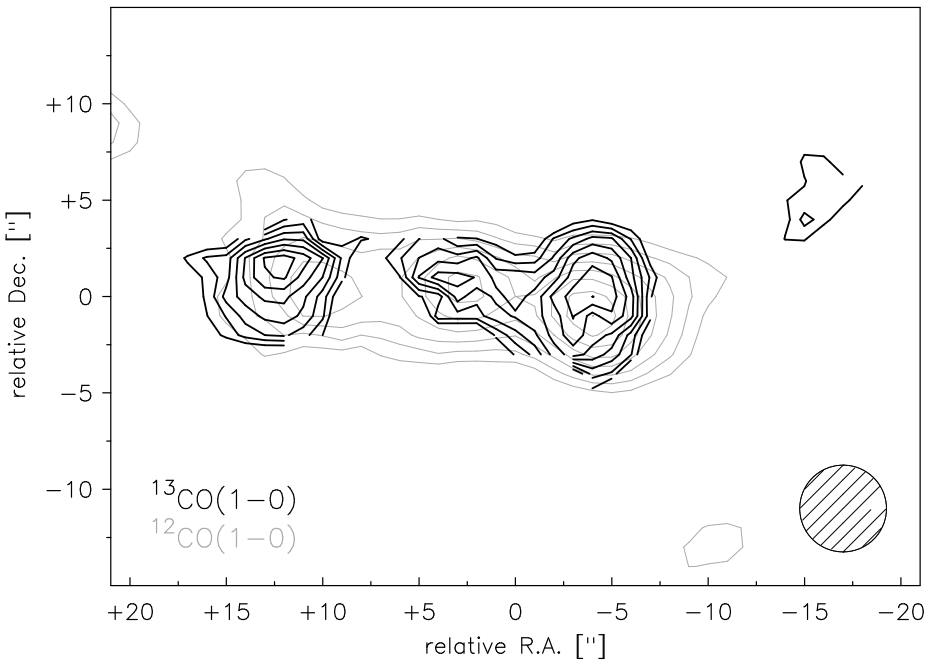

Fig. 6.— Comparison of the location of the peak emission in the ^{12}CO(1−0) (gray contours) and ^{13}CO(1−0) (black contours) in the southern arm at 4.5" resolution. The contours are in steps of 10% of the maximum value of 201 K km s^{-1} starting at 30% for the ^{12}CO(1−0) map and in steps of 20% of the maximum value of 5.0 K km s^{-1} starting at 20% for the ^{13}CO(1−0) data. All maps shown are made from the SSC data cubes.

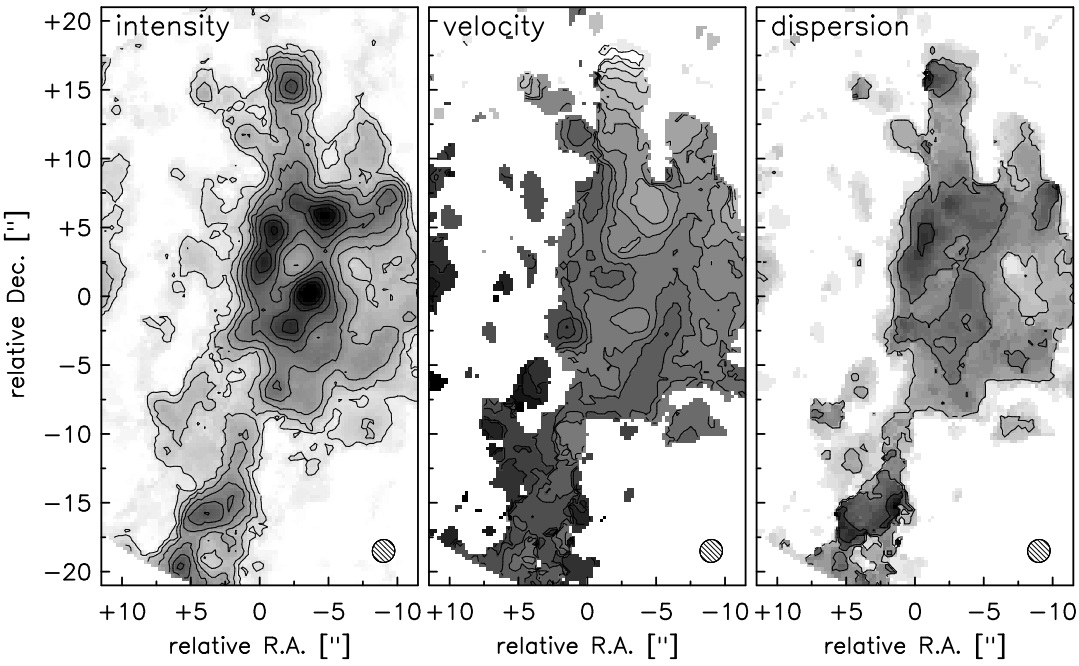

Fig. 7.— Moment maps of the ^{12}CO(2 − 1) line emission (at a resolution of 1.7"×1.5" and short spacing corrected): integrated intensity map (*left*), velocity field (*middle*), and dispersion map (*right*). The contours in the intensity map are in steps of 10% of the peak value of 23.3 Jy beam^{-1}km s^{-1}, the iso-velocity contours start at 450 km/s with steps of 5 km/s, while the contours in the dispersion map start at 5 km/s with a step of 5 km/s. The beam is shown in the bottom right corner of each panel. The angular offset is relative to the pointing center.

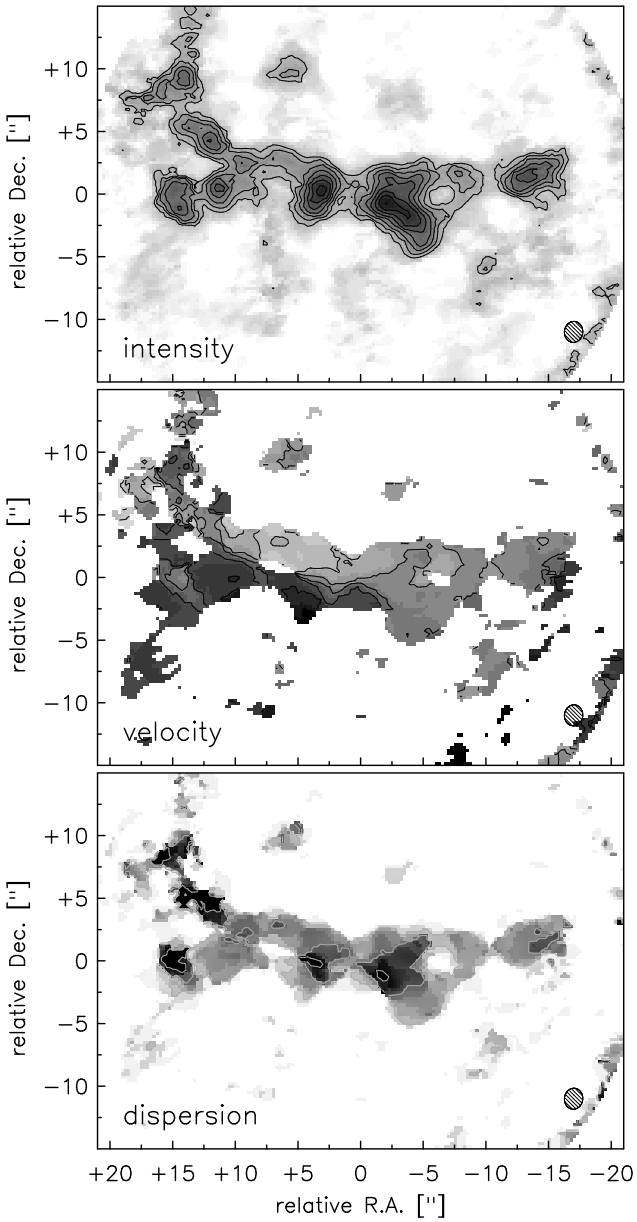

Fig. 8.— Moment maps of the ^{12}CO(2−1) line emission (at a natural resolution of 1.7"×1.5" and short spacing corrected): intensity map (*top*), velocity field (*middle*), and dispersion map (*bottom*). The contours in the intensity map are in steps of 10% of the peak value of 12.4 Jy beam^{-1}km s^{-1} starting at 30%, the iso-velocity contours start at 490 km/s with steps of 10 km/s, while the contours in the dispersion map start at 5 km/s with a step of 5 km/s. The beam is shown in the bottom right corner of each panel. The angular offset is relative to the pointing center.

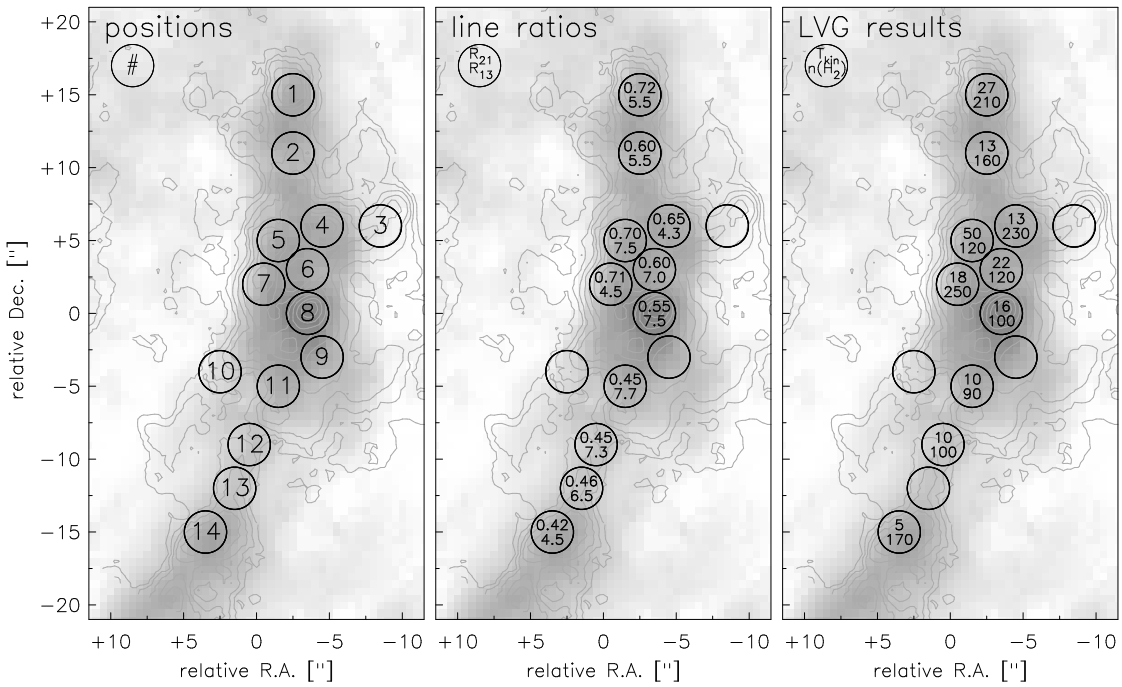

Fig. 9.— Location of the positions studied in the western arm. Numbering of the positions is given in the *left* panel where the size of the circles corresponds to a resolution of 2.9". The derived line ratios R_{21} of the $^{12}CO(2-1)$ and $^{12}CO(1-0)$ emission and R_{13} of the $^{13}CO(1-0)$ and $^{12}CO(1-0)$ emission for the individual positions is listed in the *middle* panel. Positions with empty circles have only upper limits in at least one line. The derived kinetic temperature T_{kin} and volume density of H_2 $n(H_2)$ from the LVG analysis are given in the *right* panel. The integrated $^{12}CO(2-1)$ intensity (contours) is overlaid on the $^{12}CO(1-0)$ intensity (gray-scale).

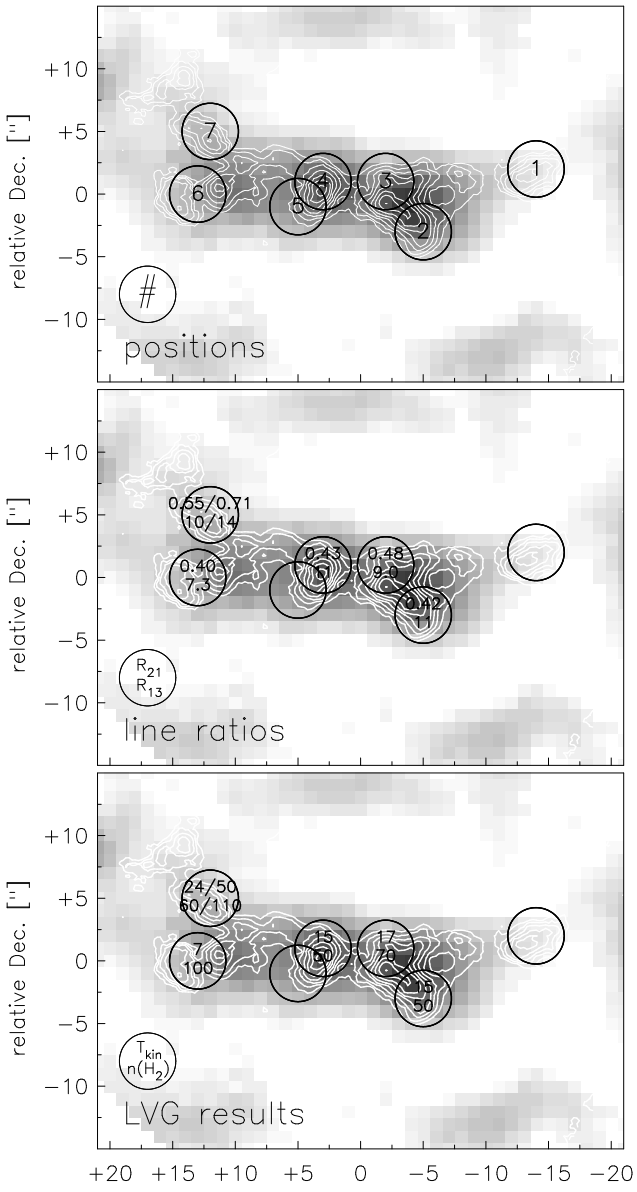

Fig. 10.— Location of the positions studied in the western arm. Numbering of the positions is given in the *top* panel where the size of the circles corresponds to a resolution of 4.5". The derived line ratios R_{21} of the $^{12}CO(2-1)$ and $^{12}CO(1-0)$ emission and R_{13} of the $^{13}CO(1-0)$ and $^{12}CO(1-0)$ emission for the individual positions is listed in the *middle* panel. Positions with empty circles have only upper limits in at least one line. The derived kinetic temperature T_{kin} and volume density of H_2 $n(H_2)$ from the LVG analysis are given in the *bottom* panel. The integrated $^{12}CO(2-1)$ intensity (contours) is overlaid on the $^{12}CO(1-0)$ intensity (gray-scale).

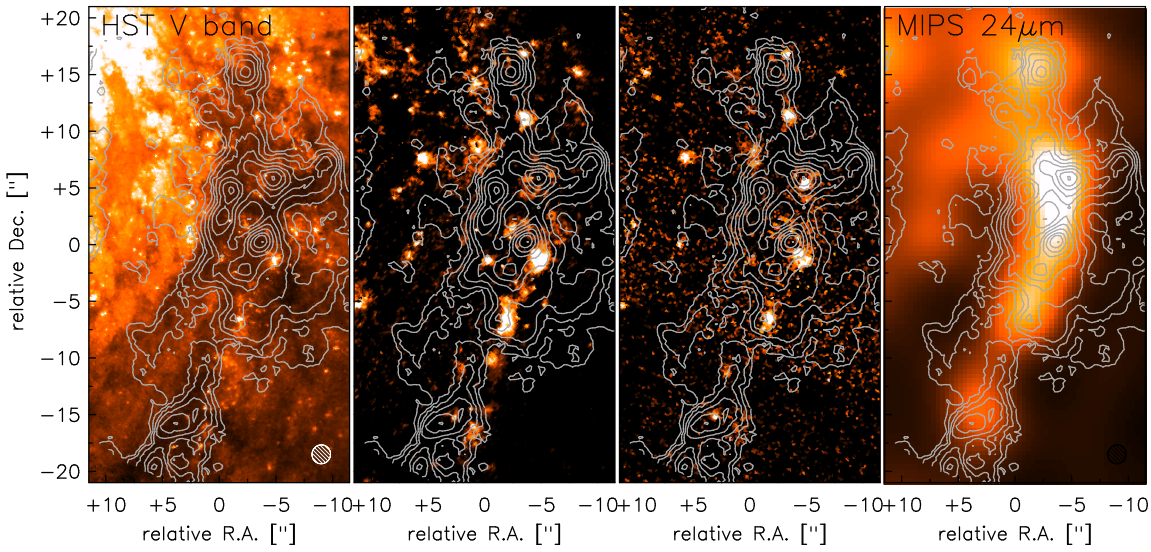

Fig. 11.— Comparison of the ^{12}CO$(2-1)$ line emission (same contours as Fig. 7) to the stellar light distribution in the HST V band (*left*) as well as the Hα (*middle left*) and Paα (*middle right*) line emission mainly arising from HII regions and the MIPS 24μm continuum emission tracing warm dust heated by young stars (*right*).

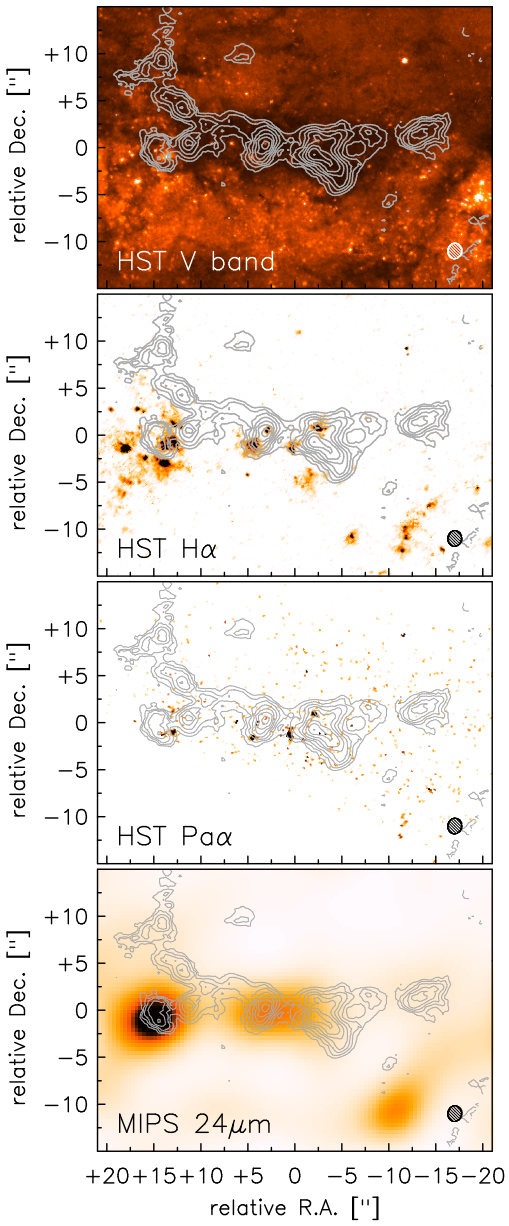

Fig. 12.— Comparison of the ^{12}CO$(2-1)$ line emission (same contours as Fig. 8) to the stellar light distribution in the HST V band (*top*) as well as the Hα (*middle top*) and Paα (*middle bottom*) line emission mainly arising from HII regions and the MIPS 24μm continuum emission tracing warm dust heated by young stars (*bottom*).

Table 1. M 51a fields

Pointing	R.A. (J2000)	Dec. (J2000)
West	13:29:50.14	+47:11:25.27
South	13:29:55.17	+47:10:47.41

Note. — Pointing centers for two selected fields in the M1 spiral arm of M 51a.

Table 2. Observations and Set-up

Pointing	Transition	Tracks	v_{LSR} ($\mathrm{km\,s^{-1}}$)	$\Delta\, v$ ($\mathrm{km\,s^{-1}}$)	# of Channels
West	^{12}CO$(2-1)$	1.5L,1E,1H	489	2.6	64
	^{13}CO$(1-0)$	1C,1L,1.5H	489	2.7	32
	C^{18}O$(1-0)$	1C,1L,1.5H	488	5.5	16
	HCN(1-0)	1C,2L,1.5H	493	6.8	16
	HCO+(1-0)	1C,2L,1.5H	493	6.7	16
South	^{12}CO$(2-1)$	1.5L,1E,1H	517	5.2	32
	^{13}CO$(1-0)$	1C,1L,1H	517	5.4	16
	C^{18}O$(1-0)$	1C,1L,1H	517	5.5	16
	HCN(1-0)	0.5C,4L,2H	523	6.8	16
	HCO+(1-0)	0.5C,4L,2H	523	6.7	16

Note. — Here we list the final spectral resolution used and the v_{LSR} of the central channel. The observed tracks are given as the number of full ($\sim 5\,\mathrm{hr}$ on-source) tracks per configuration, e.g. 1.5L = 1.5 full tracks in L configuration.

Table 3. Parameters of the OVRO Data

Pointing	Line	Weighting	rms ($\mathrm{mJy\,beam^{-1}}$)	beam ($''\times''$)
West	^{12}CO$(2-1)$	na	22	1.67×1.63
	^{12}CO$(2-1)$	ro	26	1.31×1.28
	^{12}CO$(2-1)$	un	27	1.27×1.25
	^{13}CO$(1-0)$	na	17	3.91×3.19
	^{13}CO$(1-0)$	ro	19	2.87×2.45
	C^{18}O$(1-0)$	na	13	4.22×3.77
	HCN(1-0)	na	13	4.76×3.98
	HCO+(1-0)	na	12	4.67×3.93
South	^{12}CO$(2-1)$	na	19	1.68×1.46
	^{12}CO$(2-1)$	ro	22	1.33×1.21
	^{12}CO$(2-1)$	un	25	1.28×1.20
	^{13}CO$(1-0)$	na	17	4.45×3.69
	C^{18}O$(1-0)$	na	15	4.63×4.18
	HCN(1-0)	na	12	3.88×3.28
	HCO+(1-0)	na	11	4.07×3.53

Note. — Three different values are used for weighting of the *uv* data, namely a (Briggs) robust parameter of +5 (=na; 'natural weighting'), 0 (=ro; 'robust weighting'), and -5 (=un; 'uniform weighting').

Table 4. Sensitivity of the Short Spacing Corrected Data

Pointing	^{12}CO$(1-0)$ (K)	^{12}CO$(2-1)$ (K)	^{13}CO$(1-0)$ (K)	C^{18}O$(1-0)$ (K)
West-2.9	0.32	0.13	0.28	—
West-4.5	0.23	0.08	0.09	0.08
South-4.5	0.25	0.06	0.09	0.09

Note. — The *rms* noise in the short spacing corrected data cubes of the CO transitions. All CO data cubes have the same resolution of 2.9″ (West-2.9) or 4.5″ (West-4.5, South-4.5).

Table 5. Line Fluxes and Ratios at 2.9" resolution

Position	Offset (";")	^{12}CO$(1-0)$ (K km s^{-1})	^{12}CO$(2-1)$ (K km s^{-1})	^{13}CO$(1-0)$ (K km s^{-1})	v_{50} (km s^{-1})	$\frac{^{12}CO(2-1)}{^{12}CO(1-0)}$	$\frac{^{12}CO(1-0)}{^{13}CO(1-0)}$
w1	0;+15	187	116	26	60	0.72	5.5
w2	0;+11	150	87	21	50	0.60	5.5
w3	-6;-6	87	103	$\leq$19	36	1.10	$\geq$9.5
w4	-2;+6	193	152	39	35	0.65	4.3
w5	+1;+5	219	135	14	60	0.70	7.5
w6	-1;+3	204	112	22	50	0.60	7.0
w7	+2;+2	185	137	21	46	0.71	4.5
w8	-1;0	303	157	31	40	0.55	7.5
w9	-2;-3	222	117	$\leq$23	45	0.55	$\geq$9.0
w10	+5;-4	102	65	$\leq$22	43	0.63	$\geq$7.0
w11	+1;-5	185	102	31	30	0.45	7.7
w12	+3;-9	128	64	23	31	0.45	7.3
w13	+4;-12	142	71	28	36	0.47	6.5
w14	+6;-15	215	113	47	38	0.42	4.5

Note. — Here we list the measured integrated line fluxes for the different position in the western pointing. The lower case letters refer to the 2.9″ resolution data that was used to derive the measurements. The $x-$ and $y-$offsets are relative to the pointing centers given in Tab. 1. The FWHM (v_{50}) is derived from the ^{12}CO$(1-0)$ line. The line ratios were derived from scaling the ^{12}CO$(2-1)$, ^{13}CO$(1-0)$, and C^{18}O$(1-0)$ spectra to the ^{12}CO$(1-0)$ spectrum. This method is more reliable than using the peak flux or the integrated flux in the case of low S/N data. Therefore the line ratios listed are not in perfect agreement with the ratio of the integrated line fluxes.

Table 6. Line Fluxes and Ratios at 4.5" resolution

Position	Offset (";")	^{12}CO$(1-0)$ (K km s^{-1})	^{12}CO$(2-1)$ (K km s^{-1})	^{13}CO$(1-0)$ (K km s^{-1})	C^{18}O$(1-0)$ (K km s^{-1})	v_{50} (km s^{-1})	$\frac{^{12}CO(2-1)}{^{12}CO(1-0)}$	$\frac{^{12}CO(1-0)}{^{13}CO(1-0)}$	$\frac{^{12}CO(1-0)}{C^{18}O(1-0)}$
W1	0;+15	164	91	22	≤13	64	0.63	5.1	≥15
W2	0;+11	151	77	19	10	55	0.60	5.8	17
W3	-6;+7	83	89	4	≤9	45	1.10	10	≥10
W4	-2;+6	184	127	25	7	39	0.60	6.0	25
W5	+2;+4	155	115	18	≤11	55	0.76	5.7	≥14
W6	-1;0	273	136	27	6	42	0.53	8.0	25
W7	+1;-5	170	100	18	≤7	32	0.50	9.0	≥26
W8	+5;-10	113	67	16	≤8	39	0.54	7.8	≥14
W9	+7;-16	178	100	25	≤8	39	0.45	5.0	≥22
S1	-14;+2	44	46	≤5	≤5	26	0.87	≥8.6	≥9
S2	-5;-3	147	57	11	≤6	34	0.42	11	≥23
S3	-2;+1	134	62	7	≤7	37	0.48	9.0	≥19
S4	+3;+1	166	59	5	≤9	46	0.43	11	≥19
S5A	+5;-1	45	26	≤6	≤6	30	0.52	≥7.5	≥8
S5B		86	29	≤6	≤6	30	0.37	≥9.5	≥15
S6A	+13;0	20	24	≤6	≤8	40	0.90	6.5	≥3
S6B		80	36	8	≤4	22	0.40	7.3	≥20
S7A	+12;+5	60	26	3	≤6	33	0.55	10	≥10
S7B		32	21	2	≤5	26	0.71	14	≥6

Note. — Here we list the measured integrated line fluxes for the different position in the western and southern pointing. The capital letters refer to the 4.5″ resolution data where all measurements were obtained. See caption of Tab. 5 for details.

Table 7. Results of the Large Velocity Gradient Analysis

Position	$\frac{dv}{dr}$	T_{kin} (K)		$N(H_2)$ ($10^{22}cm^{-2}$)		$n(H_2)$ (cm^{-3})		X_{CO} ($10^{20}cm^{-2}K^{-1}km^{-1}s$)	
		$\frac{dv}{dr}$=c.	vir.	$\frac{dv}{dr}$=c.	vir.	$\frac{dv}{dr}$=c.	vir.	$\frac{dv}{dr}$=c.	vir.
w1	0.4	22	27	1.5	1.7	340	210	0.8	0.9
w2	0.4	13	13	1.8	2.1	280	160	1.2	1.4
w4*	0.5	12	13	2.8	3.5	350	230	1.5	1.8
w5	0.3	35	50	1.2	1.2	250	120	0.6	0.5
w6	0.3	18	22	1.6	2.4	230	120	0.8	1.2
w7	0.5	16	18	2.1	2.6	380	250	1.1	1.4
w8	0.3	14	16†	2.9	4.5	200	100	0.9	1.5
w11	0.3	8	10†	3.2	4.3	180	90	1.7	2.3
w12	0.3	8	10	2.2	2.9	190	100	1.7	2.3
w14	0.4	5†	5†	10.9	16.6	280	170	5.1	7.7
S2	0.2	13	15†	1.4	2.6	120	50	0.9	1.8
S3*	0.3	13	17	1.3	2.0	160	70	1.0	1.5
S4*	0.2	13	15	1.5	2.9	120	50	0.9	1.8
S6B*	0.3	7†	7†	1.7	3.0	190	100	2.1	3.7
S7A	0.2	21	24	0.4	0.7	140	60	0.7	1.2
S7B[a]	0.3	43	50	0.2	0.3	260	110	0.5	0.8
< value >	0.3	16	20	2.3	3.3	240	120	1.3	2.0

[a]A $[^{12}CO]/[^{13}CO]$ abundance of 60.0 was used.

*Bright Hα emission present inside CO aperture.

†Beam filling factor > 1.

Note. — The kinetic temperatures T_{kin} and H_2 column and volume densities $N(H_2)$ and $n(H_2)$ were derived from the LVG analysis described in section 4. Typical uncertainties for the kinetic temperature are (75-100)% while the H_2 densities have uncertainties of about 25% based on the (10-15)% calibration uncertainty for the CO line data. A CO abundance of $[^{12}CO]/[H_2]$ and $[^{12}CO]/[^{13}CO]$ of 8.0×10^{-5} and 30.0, respectively, were assumed. The velocity gradient $\frac{dv}{dr}$ was either kept fixed at 1.0 $\mathrm{km\,s^{-1}}\,pc^{-1}$ or virialized gas was assumed where $\frac{dv}{dr} = 3.1\sqrt{\frac{n(H_2)}{10^4}}$. The corresponding conversion factors X_{CO} from CO line temperature to H_2 column density are also listed, the standard Galactic conversion factor is $1.8 \times 10^{20}\,\mathrm{cm^{-2}K^{-1}km^{-1}s}$ (e.g. Dame et al. 2001). The last row lists the average values of all regions analyzed.